Author: Castellanos Nash, P.
Title: Breaking & Entering : PAH photodissociation and top-down chemistry
Issue Date: 2018-06-28

II

FULLERENES IN PHOTODISSOCIATION REGIONS

Recent studies have confirmed the presence of buckminsterfullerene (C_{60}) in different interstellar and circumstellar environments. However, several aspects regarding C_{60} in space are not well understood yet, such as the formation and excitation processes, and the connection between C_{60} and other carbonaceous compounds in the interstellar medium (ISM), in particular polycyclic aromatic hydrocarbons (PAHs). In this paper we study several photodissociation regions (PDRs) where C_{60} and PAHs are detected and the local physical conditions are reasonably well constrained, to provide observational insights into these questions. C_{60} is found to emit in PDRs where the dust is cool (T_d = 20–40 K) and even in PDRs with cool stars. These results exclude the possibility for C_{60} to be locked in grains at thermal equilibrium in these environments. We observe that PAH and C_{60} emission are spatially uncorrelated and that C_{60} is present in PDRs where the physical conditions (in terms of radiation field and hydrogen density) allow for full dehydrogenation of PAHs, with the exception of Ced 201. We also find trends indicative of an increase in C_{60} abundance within individual PDRs, but these trends are not universal. This results support models where the dehydrogenation of carbonaceous species is the first step towards C_{60} formation. However, this is not the only parameter involved and C_{60} formation is likely affected by shocks and PDR age.

P. Castellanos, O. Berné, Y. Sheffer, et al. 2014, *C_{60} in photodissociation regions*, Astrophys. J., 794, 83

2.1. INTRODUCTION

Buckminsterfullerene or C_{60} was first discovered in laboratory experiments aimed to understand the spectroscopy of carbon chain molecules in the interstellar medium (ISM) and circumstellar envelopes (Kroto et al. 1985). Based on their study, the discoverers of C_{60} concluded that the molecule corresponded to a new form of carbon organized as a truncated icosahedron, usually compared with the old style black and white "soccer" ball.

C_{60} is a super-stable molecule and is considered the prototypical fullerene, cage-like molecules of pure carbon. Krätschmer et al. (1990) developed a method to produce bulk quantities of C_{60} by evaporating graphite electrodes in a helium atmosphere. They also confirmed the structure of the molecule through X-ray diffraction and its infrared (IR) spectrum. The discovery of fullerenes has also opened up the research of carbon nanotubes, another different form of carbon which combines the properties of graphite and fullerenes (Iijima 1991).

The values for the IR active modes of C_{60} are 526, 575, 1182 and 1429 cm^{-1}, which correspond to 18.9, 17.4, 8.5 and 7.0 μm (Menéndez & Page 2000). Several theoretical and experimental studies have been carried out on the IR bands of (Chase et al. 1992; Fabian 1996; Choi et al. 2000; Iglesias-Groth et al. 2011) but, while the values for the frequencies show a good agreement, reported intrinsic band strengths vary widely.

From its very discovery, C_{60} was considered a potential component of interstellar dust and was speculated to be the carrier of some of the diffuse interstellar bands (DIBs). Its survival in ISM conditions is supported by its high stability. However, until recently, unequivocal detection has not been possible. A first tentative detection was the association of two, weak, far-red absorption bands with ${C_{60}}^{+}$ (Foing & Ehrenfreund 1994). This identification has been contested and the issues were never fully resolved (Maier 1994). The main obstacle for the detection of fullerenes in emission stems from the fact that the mid-IR spectra of almost all interstellar sources are dominated by the vibrational spectrum of polycyclic aromatic hydrocarbons (PAHs). Because of this, in sources with strong PAH emission, small amounts of fullerenes are difficult to detect, with their emission hidden by the PAH bands and the continuum.

Cami et al. (2010) recognized C_{60} and C_{70} bands in the spectrum of the planetary nebula (PN) Tc 1, which has no strong PAH bands. After the detection of these transitions and their association with C_{60} several more objects have been investigated, showing that C_{60} exists in a variety of sources in different stages of stellar evolutions and with varying physical conditions. Most of these observations have dealt with PNe, including galactic and extragalactic sources in the Magellanic Clouds (García-Hernández et al. 2011; Otsuka et al. 2012), proto-PN (Zhang & Kwok 2011) and in circumstellar envelopes of binary post-AGB stars (Gielen et al. 2011). There has also been a detection towards a young stellar object (YSO) and a Herbig Ae/Be (Roberts et al. 2012), which represent isolated prestellar objects. C_{60} was also detected in photodissociation regions (PDRs), associated with both reflection nebula (RN) (Sellgren et al. 2010) and HII regions (Rubin et al. 2011).

The excitation mechanism of C_{60} is not yet clear. This is an important question to address since it determines which physical conditions of its environment are traced by the bands. Two different mechanisms have been suggested: Cami et al. (2010) consider the band ratios from Tc 1 to be consistent with a thermal distribution of the excited states, and thus derive an excitation temperature of ∼330 K. This mechanism requires C_{60} not to be in the gas phase, but in solid state or deposited on the surface of dust grains.

Another excitation mechanism, proposed by Sellgren et al. (2010), assumes that C_{60} remains in the gas phase and the bands originate from IR fluorescence. This is widely accepted as the excitation mechanism for PAHs and consists in the absorption of a single UV photon, which leaves the molecule highly excited and leads to a redistribution of the energy between the vibrational modes. While the reported 7.0/18.9 μm ratio found in NGC 7023 is in good agreement with fluorescence models, a much lower value was reported in the reflection nebula NGC 2023 (Sellgren et al. 2010). We note though that this ratio is very difficult to determine in spectra dominated by the PAH features as the underlying plateau emission is both intense and broad. This holds for NGC 7023 and NGC 2023 and the problem is compounded when the program `pahfit` is used to extract the intensity for highly blended and weak features, as the adopted intrinsic Lorentzian profile (which is inappropriate for fluorescence from highly excited species, cf. Tielens 2008) locates much of the emission in ill-fitted wings. Moreover, the analysis of observed C_{60} band ratios to discriminate between the thermal and fluorescence emission mechanism in space are hampered by the unknown intrinsic strength of these modes. Recently, Berné et al. (2013) reported a detection of ${C_{60}}^{+}$ in NGC 7023 through four bands at 6.4, 7.1, 8.2 and 10.5 μm. This would support the idea that C_{60} is in the gas-phase, at least in environmental conditions similar to those found in NGC 7023.

The formation of C_{60} is also the subject of debate. It seems self-evident to consider that C_{60} could be build-up from small (hydro)carbon chains in the C-rich ejecta of Tc 1 and other PNe whose spectra are dominated by C_{60}. In H-poor environments (not the case of these PNe), simple formation paths analogous to the chemical routes described by Kroto et al. (1985) might lead to C_{60} formation (Cherchneff et al. 2000). However, neither mechanism is efficient enough to account for the widespread detection of C_{60} in the ISM.

Another hypothetical formation route in PNe is through photochemical processing of hydrogenated amorphous carbon (HAC; Bernard-Salas et al. 2012; Micelotta et al. 2012). The details of this mechanism require the presence of large HAC clusters ($N_C >$ 100), with a high atomic hydrogen fraction (i.e. not exposed to strong or continued UV radiation). The sudden exposure of these small compounds to UV photons is speculated to lead to dehydrogenation and aromatization. This would result in giant fullerene cages which will shrink to C_{60} and C_{70} through C_2-loss.

Finally, Berné & Tielens (2012) recognized that the abundance of C_{60} increases rapidly when approaching the illuminating star of the reflection nebula NGC 7023, while the abundance of PAHs decreases. They propose that UV processing of PAHs leads to fullerene formation. Under the influence of radiation, PAHs will first become dehydrogenated, leading to the formation of graphene-like sheets. A continued exposure to high energy photons is expected to remove carbon from within the structure, which would force the formation of pentagonal rings and the bending of the sheet. This process of destruction leads to multiple different intermediate species. Because of its high stability, C_{60} is expected to be the photoproduct with the longest lifetime, and therefore it can be present at ∼0.01% of the elemental C near the star.

In this study, our goal is to contribute to the understanding of the origin and evolution of C_{60} in environments where high PAH abundance is also found. We test the formation mechanism proposed by Berné & Tielens (2012) by comparing the variations of the fractional abundance of C_{60} and PAHs as a function of physical conditions, in terms of the UV field (G_0) and the hydrogen density (n(H)). We also consider spatial variations of these abundances within the sources, in particular with respect to the position of strong sources of radiation. We used data from IRS (Houck et al. 2004) on-board of the *Spitzer Space Telescope* (Werner et al. 2004) and the PACS instrument (Poglitsch et al. 2010) on the *Herschel Space Observatory* (Pilbratt et al. 2010), for three PDRs: NGC 2023 North, Ced 201 and RCW 49. We complement this analysis by including previous observations of the Horsehead nebula, IC 63 and Orion's Veil. For these latter sources we do not perform such a detailed analysis since the C_{60} bands are not detected, except in Orion's Veil, which was studied by Boersma et al. (2012).

This chapter is organized as follows: in Sect. 2.2 we give a description of the physical and chemical conditions of the sources, taken from the literature. Sect. 2.3 describes the data from IRS and PACS that were used and explain the data reduction process. In Sect. 2.4, the reduced spectra and feature maps obtained from IRS are presented, together with the derivation of the UV field intensity from the PACS for each source. We also describe the observed variations of C_{60} and PAH abundances within each source. In Sect. 2.5 we discuss our results and compare them with the C_{60} formation model of (Berné & Tielens 2012). Finally, Sect. 2.6 summarizes the main results and conclusions of this work.

2.2. Sources

2.2.1. NGC 2023

NGC 2023 is at a distance of 330–385 pc and is illuminated by HD 37903. This star is usually classified as a B1.5 V star (Brown et al. 1994), although more recent studies have concluded that it is a Herbig Ae/Be star of spectral class B2 Ve (Mookerjea et al. 2009), based on its UV spectra and IR excess. This RN is part of the dark cloud L 1630 in Orion, which also hosts the famous Horsehead nebula (B 33). Surrounding HD 37903 there is a small HII region, with a size of 0.015 pc (Knapp et al. 1975; Pankonin & Walmsley 1976). A far-IR study by Harvey et al. (1980), showed that the molecular cloud L 1630 lies behind HD 37903. The age of the stars within NGC 2023 has been calculated to be 1–7 Myr, with the most massive stars falling towards the lower end of the range (López-García et al. 2013).

Figure 2.1 gives a general overview of NGC 2023. The shape of the reflection nebula is roughly circular, with HD 37903 located to the South-East of the center. The radiation from HD 37903 is the main source of UV photons and creates a bubble-shaped cavity, particularly clear in the IRAC 8 μm image (Fig. 2.1), which traces mostly PAH emission. Outside the cavity, PAH emission become faint, as expected due to UV ex-

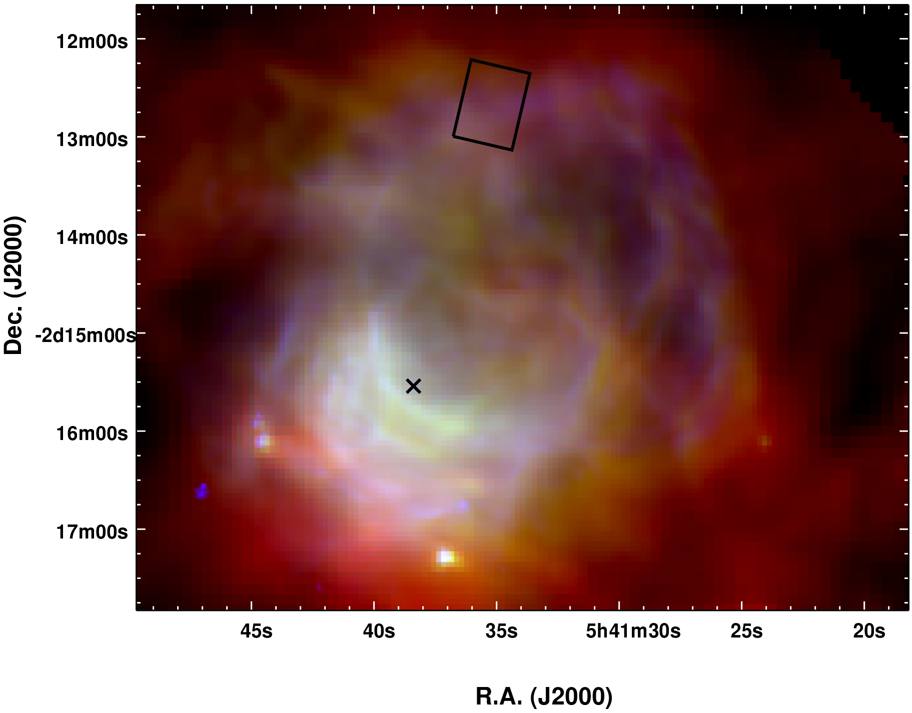

Figure 2.1.: Composite image of NGC 2023. In blue is the IRAC 8 μm image, showing the distribution of PAHs. In green is the PACS 70 μm map, which traces warm dust grains. In red is PACS 160 μm, tracing colder dust. The cross indicates the position of HD 37903 and the black box shows the IRS field that we will use for this work.

tinction. Surrounding the cavity, several filaments or ridges are observed, most clearly in PAH and warm dust emission. In particular, close to HD 37903, the southern ridge is the most luminous part of the nebula, hosting a high concentration of YSOs (Lada et al. 1991; Mookerjea et al. 2009). Other, less luminous ridges can be seen to the North and the West of HD 37903. The black box in Fig. 2.1 shows the IRS field that will be the focus of our analysis, which lies on top of the northern ridge of NGC 2023.

From observations of far-IR fine structure lines of [CII], [OI] and [SiII], Steiman-Cameron et al. (1997) established that the environment in NGC 2023 is clumpy. Their observation of the northern PDR is not spatially coincident with the position of the IRS field, but corresponds to a position closer to the HD 37903. For this location they find conditions consistent with $G_0 = 2 \times 10^4$ and $n_0 = 3 \times 10^3$ cm^{-3}. Pilleri et al. (2012) model the same IRS field we use in this study. They derive n_0 as a function of the distance to HD 37903 fitting a power law for the density profile, from the density in the diffuse region (a free parameter in their fit) up to a maximum density, which they take from Fuente et al. (1995), based on CN observations. The density ranges from 2.4×10^3 cm^{-3} to 2×10^4 cm^{-3} throughout the field.

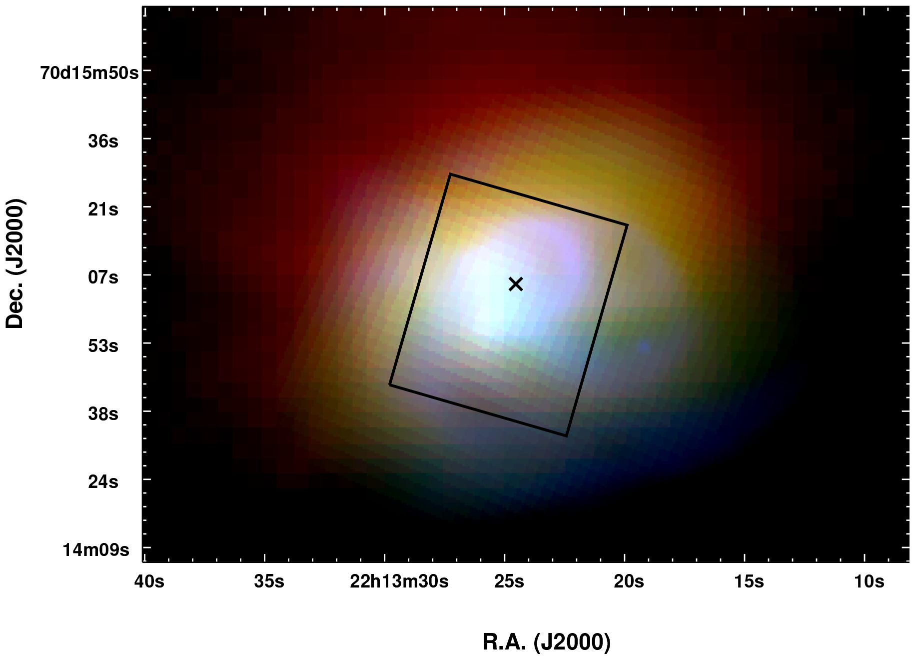

Figure 2.2.: Composite image of Ced 201. Blue corresponds to the IRAC 8 μm image, green to MIPS 24 μm and red to PACS 70 μm. The box is the IRS field that will be used in this work. The cross marks the position of the illuminating star BD +69 1231.

Sellgren et al. (2010) reported the detection of three features of C_{60} at 7.0, 17.4 and 18.9 μm in NGC 2023. A recent work by Peeters et al. (2012) also detected extended C_{60} emission — based on the 18.9 μm band — in two areas within NGC 2023, using the IRS instrument on-board of *Spitzer*. In the southern field they observed that spatial variations of C_{60} and PAHs are consistent with the findings of Berné & Tielens (2012) in NGC 7023 — i.e., C_{60} bands peak closer to the position of HD 37903 than the PAH features. However, in their northern position they find the opposite, with C_{60} peaking further away from the illuminating star than the PAHs, which they suggest may be due to geometrical effects.

2.2.2. Ced 201

Ced 201 is an unusual RN, since it is the result of a chance encounter between a molecular cloud and a runaway B9.5 V star (BD +69 1231), while in most RNe the illuminating star is formed within the cloud. This was realized due to a difference of $\sim$12 km s^{-1} in the radial velocity of the star and the molecular cloud (Witt et al. 1987). Due to its relative velocity with respect to the molecular cloud, the star in Ced 201 affects the gas and dust not only through its radiation field, but also induces shocks and turbulence. An arc-like structure can be observed to the East of the star, clear at all wavelengths shown in Fig. 2.2. This structure has been interpreted as a shock due to the star penetrating into the molecular cloud. However, no signature of a shock has been observed in the line profiles of CO (2–1) (Cesarsky et al. 2000). The cloud itself is part of the Bok Globule B 175 (L 1219), which lies at a distance of ~400 pc (Casey 1991). Given that the PDR is the product of a chance encounter, its age can be estimated using the velocity of the star with respect to the cloud. We have used the proper motion of the star (as measured by Høg et al. 2000) and calculated the angular distance from the star to the edge of the cloud in the direction of the proper motion. This gives a rough estimate of ~1500 yr.

Figure 2.2 shows the region of Ced 201. The star is entering the molecular cloud from West, generating the aforementioned arc-like structure. The cold dust (in red) — and with it the molecular cloud itself — is mostly located towards the North. Hotter dust grains, as traced by MIPS 24 μm, are found closer to BD +69 1231. PAH emission (in blue) is located much nearer to the illuminating star and to the South — the edge of the molecular cloud. PAHs and hot dust coexist in the proximity of BD +69 1231.

Young Owl et al. (2002) used far-IR fine fine structure line intensities of [CII] and [OI] (for the latter only upper limits were derived) and determined the physical conditions of the gas to be $n_0 = 4 \times 10^2$ cm^{-3} and $T_{\rm gas} = 200$ K, while for the radiation field they find $G_0 \simeq 300$. However, a previous study by Kemper et al. (1999) found higher values for both parameters, with $n_0 = 1.2 \times 10^4$ cm^{-3} and $T_{\rm gas} \simeq 330$ K. They also find $n(H_2) = (5 \pm 1) \times 10^3$ cm^{-3}. The latter values were derived from a PDR model which fits observed fine structure atomic lines (using again [CII] and upper limits of [OI]) and molecular sub-mm lines. They detected CO, ^{13}CO and HCO$^+$ and in addition put upper limits for CS and C^{18}O. The discrepancy in the values derived for the density stems from the fact that that Kemper et al. (1999) based their model not only on the fine-structure lines but also on molecular data. We expect their values to provide a better constraint on the density values. This is also supported by Casey (1991), who finds $n > 2000$ cm^{-3} based on dust emission from the far-IR.

2.2.3. RCW 49

RCW 49 is one of the most luminous and massive HII regions in the galaxy. The region is powered by the compact cluster Westerlund 2 (Westerlund 1961) where several OB stars have been detected, including at least twelve O-stars earlier than O7, with the earliest being of type O3 V((f)) (Rauw et al. 2007). It also hosts two Wolf-Rayet stars, WR20a and WR20b. WR20a was found to be a binary system of two WN6ha stars with individual masses of ~70 $M_\odot$ (Rauw et al. 2004). WR20b appears to be a single star, also with spectral type WN6ha. The presence of Wolf-Rayet stars imply a cluster age of 2–3 Myr (Piatti et al. 1998). The molecular density and kinetic temperature have been determined through CO, and ^{13}CO observations by Ohama et al. (2010), with the temperature ranging from 30 to 150 K and a typical density of $n_{\rm H_2} \simeq 3000$ cm^{-3}.

Figure 2.3 shows the environment of RCW 49. PAHs and dust are seen all over the nebula, with the brightest ridges near the Wolf-Rayet stars. The overall shape is somewhat elongated in the North-South direction, resembling a kidney. Two prominent bubbles are observed in radio continuum images, one surrounding Westerlund 2

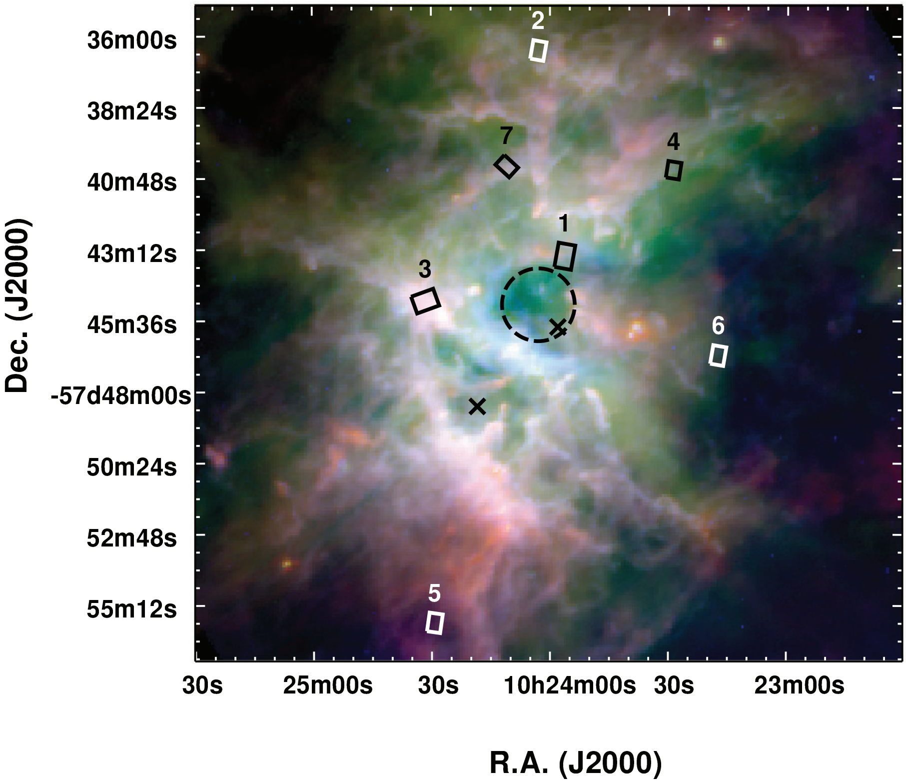

Figure 2.3.: Composite image of RCW 49. Blue corresponds to the IRAC 8 μm image, while green and red correspond the PACS images at 70 μm and 160 μm respectively. The boxes show the seven IRS fields which are used in this work. The numbers on top of each box correspond to the nomenclature used from hereon to refer to the individual regions. The crosses indicate the position of both Wolf-Rayet stars, with WR20a to the North and WR20b to the South. Finally, the dashed circle indicates the position of the cluster Westerlund 2, which hosts most of the OB stars in the region.

and the other around WR20b. The bubble around Westerlund 2 is open to the West (Whiteoak & Uchida 1997). In this region, dust and PAHs coexist with the ionized gas or are at least embedded in neutral gas mixed with the ionized region (Churchwell et al. 2004). PAH emission, traced by IRAC 8 μm (blue in Fig. 2.3), is more intense in the surroundings of Westerlund 2. The ridges, bubbles and pillars that can be seen in Fig. 2.3 are evidence of the strong interaction of the parent molecular cloud with the stellar radiation and winds from Westerlund 2 and recently formed stars. The seven IRS fields considered in this work cover regions with very different conditions, allowing us to probe a large range of UV field intensities. In the following, when we refer to individual positions we will use the numbers shown above the respective box in Fig. 2.3.

The distance to RCW 49 has been the subject of debate, with derived values ranging from 2.3 to 7.9 kpc (Brand & Blitz 1993; Whiteoak & Uchida 1997; Moffat et al. 1991), where the lower limit comes from radio continuum observations and kinematic studies and the upper limit is derived from the luminosity distance. A recent photometric analysis by Carraro et al. (2013) derives the reddening and extinction curves towards several members of Westerlund 2. With this, they correct the apparent distance modulus in order to obtain the distance to the cluster, $d = 2.85 \pm 0.43$ kpc.

2.2.4. Additional sources

In this study we also consider results involving Orion's Veil, NGC 7023, IC 63 and the Horsehead nebula. The first two sources have been previously studied and show the presence of C_{60} bands (Boersma et al. 2012; Berné & Tielens 2012). In the case of Orion's Veil eleven positions were observed (Boersma et al. 2014), which are labeled with increasing distance to Orion's Bar as I4–I1, M1–M4 and V1–V3, respectively. From these, we do not include in our analysis the two regions closest to the Bar (I4 and I3) given that their counterparts in PACS observations suffer strong contamination with emission from the Bar. We also discard the farthest region (V3), as it looks edge-on to the back of the PDR, and thus does not probe the same environment as the remaining regions (Boersma et al. 2012). The Horsehead nebula and IC 63 do not show C_{60} emission bands. In the case of the Horsehead, we have used data corresponding to the "mane", where no excess emission over the continuum is detected at $\sim$19 μm (the strongest C_{60} feature). We consider as upper limits the highest value that could be fitted using `pahfit`, although it was always fitted as a detection below 3σ. For IC 63, there are areas where there is emission over the continuum that cannot be fitted by the [SIII] line alone (which partly overlaps with the 18.9 μm band of C_{60}). These pixels are fitted by `pahfit` with confidence over 3σ but, upon visual inspection, we find that the fit is of poor quality and we consider the C_{60} band intensity to be an upper limit. Physical conditions for these additional sources will be discussed in Sects. 2.4.3 and 2.4.4.

2.3. Data

2.3.1. IRS Data

We used data from the Infrared Spectrograph (IRS; Houck et al. 2004) on-board of the *Spitzer Space Telescope* (Werner et al. 2004). The spectrograph consists of four modules, divided according to the wavelength coverage and resolution: short wavelengths with low resolution (SL), long wavelengths with low resolution (LL), short wavelengths with high resolution (SH) and long wavelengths with high resolution (LH).

For the low resolution modules the wavelength coverage goes from 5.2 μm to 38.0 μm for the combination of SL and LL and have a spectral resolution ($R = \lambda/\Delta\lambda$) between 60 and 130. In the case of the high resolution modules, the combined coverage of SH and LH ranges from 9.9 μm up to 37.2 μm, with a spectral resolution $R \simeq 600$.

We gathered the spectral cubes from the Spitzer Heritage Archive[1]. For NGC 2023 and Ced 201 we used observations from the program with PID 3512 (PI C. Joblin). In the case of NGC 2023, we considered observations performed with SL and LL modules with AOR keys 12014848 and 12011264, respectively. For Ced 201 we selected again SL and LL modules, in this case with AOR keys 11047936 and 11047680 respectively.

For RCW 49 we have 7 fields, all of them in SH module, from the program with PID 20012 (PI M. Wolfire). Their respective AOR keys are 13812992, 13813248, 13813504, 13813760, 13814016, 13814272 and 13814528. These regions are not contiguous and will be referred to according to the numbers shown in Fig. 2.3.

The data reduction and cube generation was performed using the `cubism` software (Smith et al. 2007a). The recommended data reduction begins by taking a background when available. None of the observations has a dedicated background observation. The low resolution modes have "outrigger" slits, that fall outside the area of interest. In the case of Ced 201 this slit falls on an empty patch of sky so we used this to do the background subtraction. In the observations of NGC 2023 the slit falls in regions with important emission from the same source, leading us not to consider it a background for this source. For of NGC 2023 and RCW 49 the lack of background is not detrimental, given that both sources are bright.

2.3.2. PACS Data

In order to have a measure of the far-IR (FIR) intensities we used photometric data from the Photodetector Array Camera and Spectrometer (PACS; Poglitsch et al. 2010) on-board of the ESA *Herschel Space Observatory* (Pilbratt et al. 2010). In all three sources we retrieved the available data at 70 and 160 μm from the Herschel Science Archive[2]. The observations of NGC 2023, Ced 201 and RCW 49 have respective OBSIDs of 1342227049/50, 1342196809/10 and 1342255009/10.

2.4. Analysis

2.4.1. Spectral fit

In order to fit the different features of the IRS spectra we used the tool `pahfit` (Smith et al. 2007b). This tool fits a stellar continuum and multiple modified blackbody emission curves with different temperatures. These emission curves are used to fit the mid-IR continuum, but their temperatures do not accurately represent the temperature of the dust, since grains emitting at these wavelengths are not in equilibrium with the radiation field, but are rather transiently heated to high temperatures (Draine 2003). It also considers several unresolved atomic lines as well as H_2 rotational lines. Finally it fits different PAH features and the 18.9 μm feature of C_{60}.

In Fig. 2.4 we present an example of a low resolution spectrum from NGC 2023 from the area where the 18.9 μm feature peaks. The fit matches reasonably well the

[1] http://sha.ipac.caltech.edu
[2] http://herschel.esac.esa.int/Science_Archive.shtml

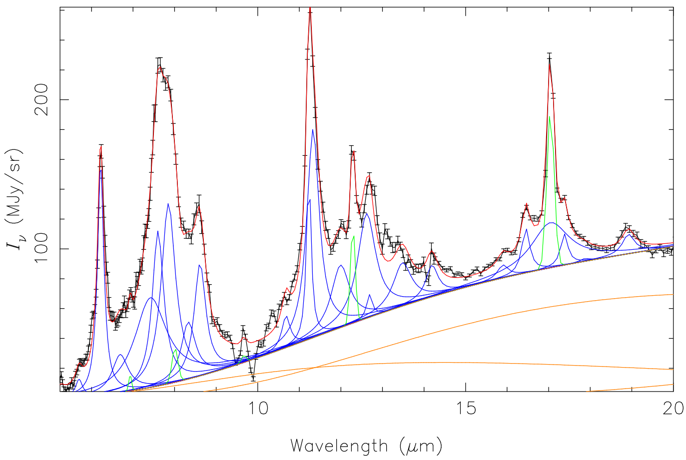

Figure 2.4.: Examples of a fitted low resolution spectrum of NGC 2023. The black line with error bars is the observed spectrum while the red line is the total fitted spectrum. The individual components are shown in blue (PAH and C_{60} features), green (unresolved H_2 lines) and orange (modified black body continua).

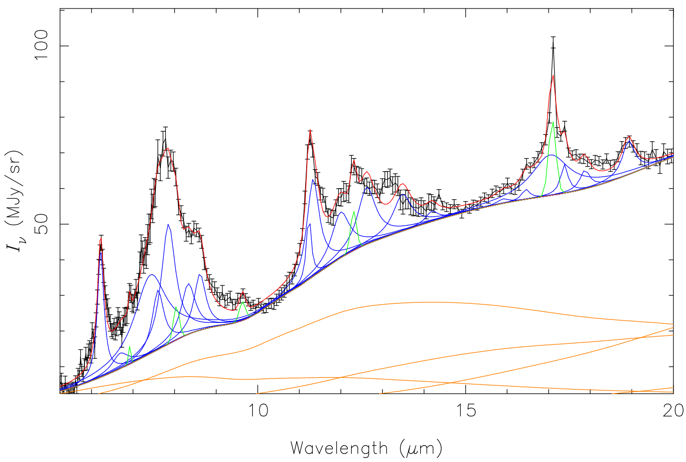

Figure 2.5.: Example of a fitted low resolution spectrum from Ced 201. The black line with error bars is the observed spectrum while the red line is the total fitted spectrum. The individual components are shown in blue (PAH and C_{60} features), green (unresolved H_2 lines) and orange (modified black body continua).

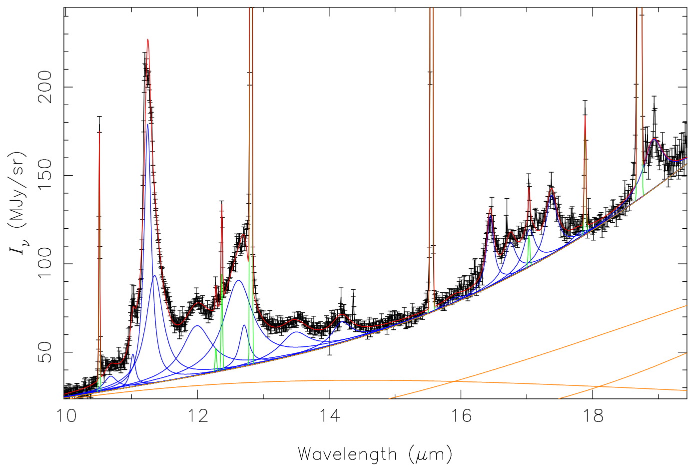

Figure 2.6.: Example of fitted a high resolution spectrum from RCW 49, Region 2. The black line with error bars is the observed spectrum while the red line is the total fitted spectrum. The individual components are shown in blue (PAH and C_{60} features), green (unresolved H_2 and atomic lines) and orange (modified black body continua).

observed spectrum with the exception of the PAH bands between 13 and 14 μm, for which the peak positions seem to be somewhat different from the values considered by `pahfit`. However, these bands are rather weak and when considering the integrated PAH band intensities their contribution will be small. The same is observed in the sample spectrum of Ced 201 (Fig. 2.5). In both sources the 18.9 μm feature associated with C_{60} is clearly present. The only unresolved lines fitted in these spectra are from H_2 pure rotational lines.

The main PAH bands at 6.2, 7.7, 8.6, 11.2, 12.7 μm and the plateau at 17.0 μm are also prominent. This allows us to consider in our analysis a pixel by pixel comparison of the variations of C_{60} and PAHs. There are however some residual problems for the PAH bands: for instance, in NGC 2023 there is a dip around 10 μm which may due to saturation of the peak-up array as described in the IRS handbook[3] (their Sect. 7.3.5). In both sources the issues are not relevant for the analysis since we focus on individual bands as fitted by `pahfit` and no such feature falls within the problematic wavelength range.

The total intensity of the 18.9 μm band is underestimated by the fit in some pixels. This issue is observed in NGC 2023 in pixels that lie to the South of the field. The origin of this problem comes from the continuum in these pixels, which drops above 20 μm and is not properly fitted, thus affecting the fit of the 18.9 μm band. In order to circumvent this issue and check the accuracy of the fit in other pixels, we consider a local linear continuum around 18.9 μm and later fit a Drude profile for the band itself. This procedure confirms that the difference between the result of `pahfit` and our fit of the 18.9 μm band is only significant in the aforementioned region. For these pixels,

[3]http://irsa.ipac.caltech.edu/data/SPITZER/docs/irs

we use the result from our local fit rather than that of `pahfit`. Other bands in this area are not significantly affected by the misplaced continuum.

One difference between the NGC 2023 and Ced 201 is the band-to-continuum ratio. The PAH bands in Ced 201 have significantly lower intensity with respect to the continuum than those in NGC 2023. This is not the case for the 18.9 μm C_{60} band, which has a similar band-to-continuum ratio in both sources. While hard to disentangle from the H_2 $S(1)$ line and the 17.0 μm plateau, the 17.4 μm band also seems to have rather similar band-to-continuum ratios in both sources. This is indicative of a large contribution of C_{60} to this interstellar band (Sellgren et al. 2010; Berné & Tielens 2012; Peeters et al. 2012).

The high resolution spectra were also analyzed using `pahfit`. However, we must note that `pahfit` was created and optimized for fitting low resolution spectra, such as the ones considered here for Ced 201 and NGC 2023. In the case of RCW 49, the spectra were taken in SH mode for all regions considered here. This forced us to change the input parameters in `pahfit`: for the unresolved atomic and molecular lines we have changed the width of the Gaussian functions used, in order to match the improved resolution of the SH mode and we have modified some of the PAH band parameters to improve the fit.

The fitting procedure follows the same principle as in the low resolution mode. Besides the aforementioned modifications of some of the parameters, we also removed all features that fall outside the range covered by the SH mode since this causes problems with the fitting routine. If this last modification is not implemented then the wings of the adopted Drude profiles of the out-of-range PAH bands are sometimes fitted as part of the continuum.

The modified fitting routine runs into problems when the band-to-continuum ratio decreases. This is the case for region 1 in RCW 49. Specially at longer wavelengths, the fit either over- or underestimates the continuum, resulting in poor fits for the 18.9 μm band. Furthermore, the 18.9 μm band is not recognizable in the spectra of this region. The continuum at this wavelength is very strong and, as such, an 18.9 μm band with intensity comparable with the highest value detected within other regions would not be noticeable. For this reason, we have decided to exclude region 1 from the rest of this study.

We looked for other potential errors in the continuum fits but, outside region 1, all fits are consistent with the data. In Fig. 2.6 we present an example of region 2 in RCW 49, which shows the strongest 18.9 μm band. The 18.9 μm band varies in intensity among the different regions, but can be recognized in the spectrum of most pixels. In some instances the detection is only marginal, but in our final analysis we exclude all points with detection below 3σ with respect to the error bars given by `pahfit`.

2.4.2. Spectral maps

Once the spectrum for each pixel have been fitted, we build intensity maps of each of the PAH bands, the spectral lines and the 18.9 μm band. We also create maps of the error bars, as derived by `pahfit`. These maps give the integrated intensity of each spectral feature and constitute the basis of our study. We restrict our analysis to areas

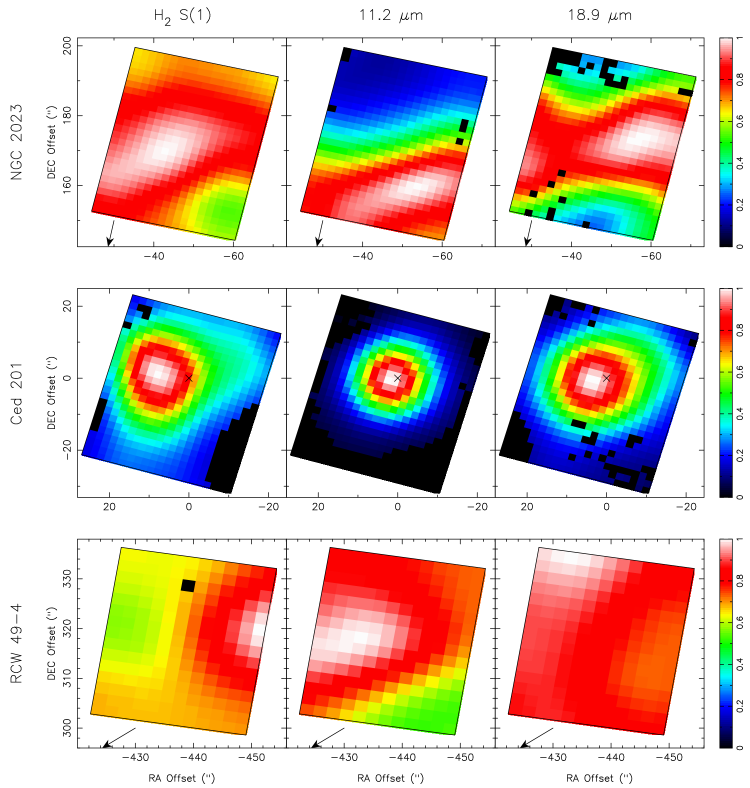

Figure 2.7.: Intensity maps of the selected spectral features: H_2 0–0 $S(1)$ line, 11.2 μm PAH band and 18.9 μm C_{60} band, all convolved to the PACS 70 μm beam. The top panels correspond to NGC 2023, the middle ones to Ced 201 and the bottom panels to Reg. 4 in RCW 49. The color scale is normalized with respect to the maximum intensity in the corresponding frame. The offsets are with respect to the position of the illuminating star, shown with a cross or pointed towards using arrows (for RCW 49 we chose the position of WR20a).

with confident detections, and thus we have flagged pixels in which the fitted intensity falls below a 3σ noise level. Finally, in order to get smoother images and correct for cases in which particular pixels have large differences in flux with respect to its neighbors, we performed a median filter with a 2×2 kernel.

In Fig. 2.7 we show maps of the 11.2 μm PAH band, the 18.9 μm band corresponding to C_{60} and the H_2 0–0 $S(1)$ line at 17.0 μm in NGC 2023, Ced 201 and region 4 of RCW 49. In all cases the PAH band peaks closer to the illuminating star than the C_{60} or H_2 lines. This contrasts with the observations on NGC 7023, where C_{60} peaks closer to the illuminating star than the PAHs.

In NGC 2023 we identify a bar-like structure in all the maps, running from the South-East to the North-West. However, the exact position of the bar varies: on the 11.2 μm map it is displaced to the South when compared to the 18.9 μm or H_2 $S(1)$ maps. Other variations observed in the bar concern the position of the peak intensity, with 18.9 μm displaying two peaks located towards the North-West and South-East of the bar, while H_2 $S(1)$ shows one peak located roughly in the middle of the bar and 11.2 μm showing also one peak, but displaced to the North-West.

The maps of Ced 201 show a clear asymmetry in the cases of the H_2 and C_{60} maps. This asymmetry is also present but in a less prominently in the PAH maps. In both the H_2 and C_{60} maps, the arc at the North-West appears much more clearly than in the PAH maps. Additionally, the peak intensity appears to the North-East of the star, in the position of the molecular cloud as shown in Fig. 2.2. In contrast, the PAH features are centered near the star and, for the 8.6 and 7.4 μm features, the spatial coincidence with IRAC 8 μm is very clear.

In RCW 49, the H_2 peak does not coincide the peak of the PAH bands, and is typically found further with respect to the illuminating star. The 18.9 μm maps shows only minor variations in intensity in most regions. As is the case for NGC 2023 and Ced 201, the 18.9 μm maps show a spatial distribution clearly different to that of the PAH maps in all the regions. In RCW 49, all PAH maps follow a similar pattern within each region, with only small changes in peak position and relative strengths. The PAH and C_{60} morphology show a superficial resemblance in a few regions, but the relative strength of the different components is very different.

In summary, in all sources where we detect the 18.9 μm band, its spatial distribution is noticeably different with respect to that of the PAH bands. Although the different PAH bands show spatial variations with respect to each other, they resemble each other much more closely than the 18.9 μm band. In most cases, the peak intensity of the C_{60} band is seen farther from the central star than the PAH bands. This behavior is the opposite of what is observed in NGC 7023 (Berné & Tielens 2012) and, in principle, does not seem to support the formation of C_{60} by UV processed PAHs. However, this divergence is seen purely from the point of view of projected distance and may not speak of the actual differences in physical conditions. As it has been suggested that the formation of C_{60} in the ISM starts with the dehydrogenation of PAHs — which is a balance between UV photolysis and reactions with H — we will consider in the next two subsections the intensity of the local radiation field and the hydrogen density.

2.4.3. UV field calculation

Considering that PAH and C_{60} are stochastically heated by UV-photons a measure of the UV field intensity is needed in order to derive proper abundances. The intensity of their respective mid-IR bands is proportional to the product of the column density of PAHs and C_{60} with the UV field intensity.

We determine the UV field intensity in terms of G_0 (1.6×10^{-3} erg cm^{-2} s^{-1}; Habing 1968) from the FIR spectrum of dust. Considering that, in a PDR, nearly all the UV radiation is absorbed by dust and then re-emitted in the FIR and assuming that grains act like a modified black body (Tielens 2005, Sec. 9.7) we have,

$$G_0 = 8.3\times10^{3}\frac{V}{\ell S}\tau_{\nu_0}\nu_0^{-\beta}\int \nu^{\beta}B(\nu,T_{\rm d})\mathrm{d}\nu, \tag{2.1}$$

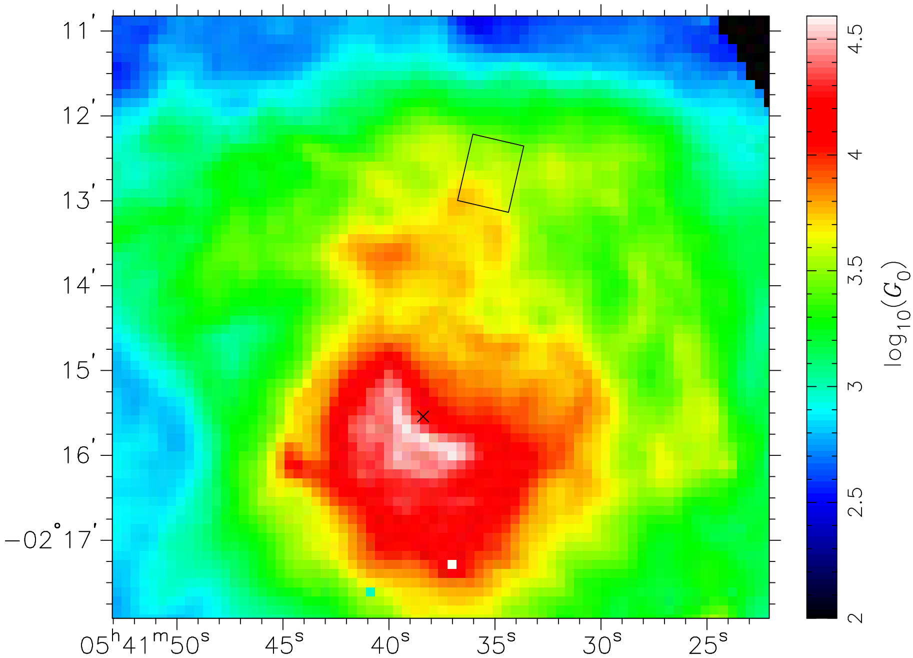

Figure 2.8.: Map of G_0 calculated from the FIR intensity for NGC 2023 with an assumed a spherical geometry, thus setting $V/\ell S = 1$. The cross shows the position of the illuminating star and the square the position of the IRS field.

where ν_0 is a reference frequency where the optical depth is τ_{ν_0}, β is the spectral index and T_d is the dust temperature. The factor $V/\ell S$ accounts for the geometry of the cloud, with S being the surface area facing the illuminating star, V the volume of the cloud and ℓ corresponding to the length along the line of sight. One issue with this calculation is that the three-dimensional geometry is generally not well known, introducing uncertainties. For example, for an edge-on disk the geometric factor would be equal to the ratio of the disk thickness over ℓ, while for a sphere this factor is equal to one. Since this method relies on the emission from dust, it will underestimate the value of G_0 in regions devoid of dust. In the three PDRs considered here the environment is dusty and the IRS fields are away from hard sources of radiation, so we expect our G_0 estimate to provide a reasonable approximation.

To calculate the total FIR intensity we use the PACS images at 70 and 160 μm from each source. For this, we first matched the 70 μm images to the 160 μm resolution and use the intensity of each pixel to fit a modified black-body to these two wavelengths. The free parameters are the dust temperature, T_d, and the optical depth τ_{ν_0}. We fixed ν_0 at 1000 GHz and considered $\beta = 1.7$. The value of β in the ISM is usually found to be somewhere between one and two, with a slight dependence on the dust temperature (Dupac et al. 2003). It has been observed that for $T_d \lesssim 20$ K, $\beta \simeq 2$, while for $T_d \gtrsim 30$ K a value of $\beta \simeq 1.5$ is found (Shetty et al. 2009). We chose an intermediate value since

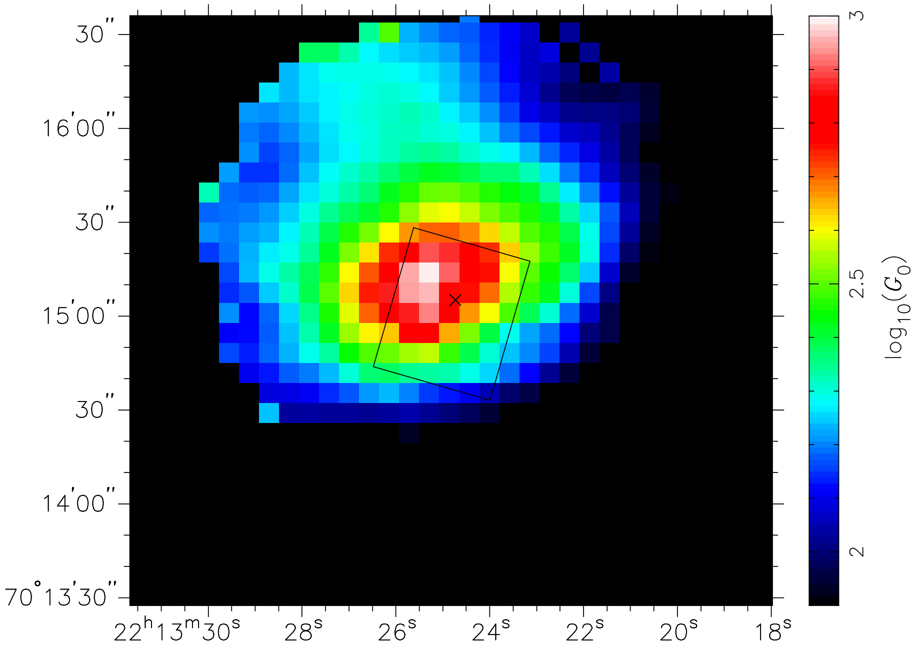

Figure 2.9.: Map of G_0 calculated from the FIR intensity for Ced 201 assuming spherical geometry ($V/\ell S = 1$). The cross shows the position of the illuminating star and the square corresponds to the IRS field.

in all sources we expect dust with temperatures in both regimes. We are not fitting β directly since we only have two points for our fit which is not enough to realistically fit three parameters. To make the fit we used a Levenberg-Marquardt fitting routine. With this fit, we derive the value of T_d and τ_{ν_0}, which we use to determine G_0.

We assumed spherical geometry in the three cases. For NGC 2023 (Fig. 2.8) this is likely a good assumption since the RN is almost circular, even though it is not exactly centered on the illuminating star. An additional correction factor must be added in eqn. 2.1 to account for the fact that, particularly for B-type stars, a significant part of the photons radiated have energies lower than 6 eV, that can heat the dust but do not correspond to the UV field as defined by G_0. Based on the spectral type we use a factor of 0.7 for the fraction of the stellar luminosity falling in the range between 6 and 13.6 eV (Steiman-Cameron et al. 1997). We check our calculation against the result of Sheffer et al. (2011). They found $G_0 = 1.7 \times 10^4$ in NGC 2023 S, while the region we are focusing on is about 2.3 times farther out. This is equivalent to a geometric dilution factor of 5.3, leading to $G_0 = 3200$, which is in agreement with the values seen in Fig. 2.8.

In the case of Ced 201 (Fig. 2.9) the spherical cloud assumption is not entirely realistic since the PDR is due to a chance encounter with the molecular cloud and thus the star is situated at the edge of the cloud. In this case the peak of G_0 is displaced from

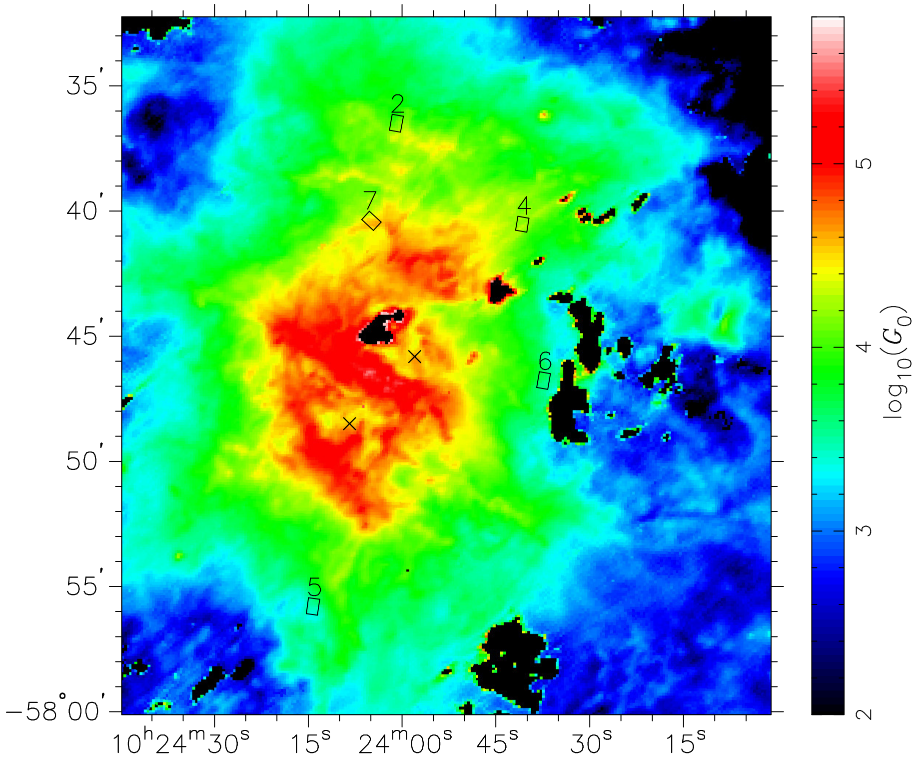

Figure 2.10.: Map of G_0 calculated from the FIR intensity for RCW 49 assuming spherical geometry ($V/\ell S = 1$). The crosses show the position of the illuminating stars and the squares the position of the five IRS fields for which we have density estimates.

the illuminating star and, furthermore, the region with highest G_0 corresponds to the arc structure seen North-East from BD +69 1231 in the molecular cloud, with much less intensity to the South-West. Due to its type, the fraction of the stellar luminosity emitted between 6 and 13.6 eV corresponds to 0.3 (Young Owl et al. 2002).

In RCW 49 (Fig. 2.10), the exact three-dimensional geometry is not well known, but it looks approximately circular and we expect that the spherical approximation will not introduce large errors. We will take into account in our discussion the possible effects that arise from changing the geometrical factor. Since the illuminating source of RCW 49 is dominated by the O-type stars we consider a factor of one for the fraction of the luminosity emitted in the far-UV. In reality, a significant fraction will be emitted at wavelengths shorter than 13.6 eV in this case, but these photons are absorbed and downgraded in the HII region.

For the additional PDRs included in this work we only used the the far-IR calculation of G_0 for Orion's Veil, resulting in G_0 ranging from $\simeq$ 30000 for the I2 field (the closest to the Bar) to ~3000–5000 for the fields that lie farther from the Bar. For NGC 7023 we used the values derived by Berné & Tielens (2012), which result in $G_0 = 10000 \pm 7000$

at the peak of the 18.9 μm band. The Horsehead nebula was studied by Abergel et al. (2003), who find $G_0 \sim 100$. For IC 63 we use the estimate of Jansen et al. (1994), which gives $G_0 \sim 650$.

Finally, comparing Figs. 2.1–2.3 against Figs. 2.8–2.10, the general structure seen in the composite images is clearly apparent in the G_0 distribution. The G_0 maps show the most characteristic features in the case of each PDR, such as the southern and northern ridges in NGC 2023, the bright bar observed in RCW 49 between the positions of WR20a and WR20b and the arc-like structure seen in Ced 201 to the North-East of BD +69 1231. The derived dust temperatures inside the IRS fields of the three PDRs range between 20 and 40 K, which is much too low for emission to be due to C_{60} embedded in grains.

2.4.4. The atomic hydrogen density

In order to estimate the variations in abundance of PAHs and C_{60} with respect to the physical conditions of each source we need to derive the atomic hydrogen densities, n(H), for each region. We estimate these based on previous studies and we derive a single value as representative for each of the regions we consider. A summary of the results for each field is presented in Table 2.1.

For NGC 2023 we base our estimate on the densities calculated by Pilleri et al. (2012). Their model uses a varying density inside the IRS field, which ranges from 2.4×10^3 cm^{-3} to 2×10^4 cm^{-3}. We consider their value for the density of the inner part of the field, since it dominates the emission.

In the case of Ced 201 we base our estimate of n(H) on the values for total hydrogen density and molecular densities from Kemper et al. (1999) and Young Owl et al. (2002). The G_0 value derived from the IR measurement is in good agreement with the value derived from the PDR/molecular cloud analysis of Kemper et al. (1999). As they included more reliable density tracers, we have adopted their value for n(H) and the IR derived value for G_0.

In RCW 49 we calculate the density based on an analysis of rotational lines of molecular hydrogen. The H_2 rotational line emission is modeled following the procedure outlined in Sheffer et al. (2011). The IRS SH observations mentioned in Sect. 2.3.1 are used to derive the H_2 0–0 $S(1)$ to $S(4)$. We additionally use LL observations to cover the H_2 0–0 $S(0)$ line. PDR models are used to fit each field individually, giving H_2 column densities and reference values of n_0. For a typical PDR, hydrogen in the surface layer is predominantly atomic and we have $n(\mathrm{H}) = n_0$. In dense PDRs, however, the H/H_2 transition is pulled to the surface and the atomic fraction varies from 1 to 10^{-3}. For our sources, this seems to apply in RCW 49 regions 2 and 4. For these two positions, we hence adopted the atomic H fraction at $A_V = 0.5$; $f_{\mathrm{H}} = 10^{-3}$ and 10^{-1} for regions 2 and 4 respectively. It must be noted that these values are highly uncertain.

The value derived for NGC 7023 by Berné & Tielens (2012) is of $n(\mathrm{H}) = 150 \pm 100$ cm^{-3}. For Orion's Veil, we estimate n(H) by using the electron densities derived from [SII] optical lines by Rubin et al. (2011). From their values we use a factor 20 to derive the neutral density (Tielens 2005). In the Horsehead nebula, Abergel et al. (2003) estimate the density just behind the ionization front to be 8×10^3 cm^{-3}. Finally,

Table 2.1.: Average physical conditions and C_{60} fractions.

Region	n(H) (cm^{-3})	G_0	G_0/n(H)	$f_{C,C_{60}}$ ($\times 10^{-5}$)	Ref.
NGC 2023	2.4×10^3	5200 ± 200	2.1	4.2	1
Ced 201	1.2×10^4	600 ± 60	0.050	44	2
RCW 49-2	4.0×10^3	11000 ± 1300	2.7	13	3
RCW 49-4	1.0×10^4	20000 ± 3000	2.0	7.2	3
RCW 49-5	2.5×10^4	3000 ± 400	0.12	11	3
RCW 49-6	2.5×10^4	5100 ± 300	0.21	12	3
RCW 49-7	2.5×10^4	34000 ± 2500	1.4	5.5	3
NGC 7023	1.5×10^2	10000 ± 7000	60	9.9	4
Veil-I2	8.7×10^3	31000 ± 1900	3.6	56	5,6
Veil-I1	8.1×10^3	22000 ± 500	2.7	41	5,6
Veil-M1	5.1×10^3	15000 ± 600	2.9	36	5,6
Veil-M2	5.1×10^3	13000 ± 600	2.5	32	5,6
Veil-M3	5.1×10^3	8700 ± 400	1.7	29	5,6
Veil-M4	3.4×10^3	5400 ± 200	1.6	30	5,6
Veil-V1	1.7×10^3	3500 ± 100	2.0	35	5,6
Veil-V2	2.6×10^3	5200 ± 100	2.0	31	5,6
Horsehead	8.0×10^3	~100	0.013	<4.3	7
IC 63	3.0×10^3	~650	0.22	<6.0	8,9

For NGC 2023, Ced 201, RCW 49 and the Veil, the values of G_0 were calculated following the procedure described in Sec. 2.4.3. Other values of G_0 and n(H) are taken from the given references. For NGC 7023 we use lower limits for G_0 and present the values at the peak of C_{60} abundance.
(1) Pilleri et al. (2012); (2) Kemper et al. (1999); (3) This work; (4) Berné & Tielens (2012); (5) Boersma et al. (2012); (6) Rubin et al. (2011); (7) Abergel et al. (2003); (8) Jansen et al. (1994); (9) Thi et al. (2009).

in the case of IC 63, we consider the results from Thi et al. (2009), who give a range from 1000–5000 cm^{-3} for the PDR density.

For all the PDRs considered here, the values of n(H) carry uncertainties that are difficult to estimate. Since we are using a single value as representative for each region, we have that the variations of G_0/n(H) within each field will be representative of variations of G_0 only.

2.4.5. Carbon fraction variations

In this section we present results of the variations in abundance of both PAHs and C_{60}. We calculate the abundances from the ratio of intensity of PAHs and C_{60} with respect to G_0, which in turn is related to the FIR intensity of large dust grains. Assuming that PAHs, C_{60} and dust compete for the same photons, we follow Tielens (2005, Sec. 6.7), and use,

$$f_C = 0.23 \left(\frac{7 \times 10^{-18}\ \mathrm{cm}^2}{\sigma_{\mathrm{FUV}}} \right) \frac{f_{\mathrm{IR}}}{1 - f_{\mathrm{IR}}}, \tag{2.2}$$

where f_{IR} is the ratio of the PAHs or C_{60} total intensities to the total IR intensity (Berné & Tielens 2012, given by eqn. 2.1 for the FIR and adding the contributions from PAHs and C_{60}, following), σ_{FUV} is the far-UV absorption cross section per carbon atom of the species under consideration. Finally, f_C is the fraction of elemental carbon locked in the species considered, which is in turn related to the total abundance.

In this calculation, we consider the total PAH intensity as the addition of all the PAH bands below 15 μm. For NGC 2023 and Ced 201 this includes features starting from $\lambda = 5$ μm. In the case of RCW 49, NGC 7023 and Orion's Veil our coverage is limited to the range between 10–15 μm since the data in these cases have been recorded using the SH mode. Considering the contribution that this range has to the total PAH intensity in NGC 2023 and Ced 201 we find that it is fairly constant fraction at ~ 0.2. We use this value as a correction factor in order to estimate the total PAH abundance in RCW 49, NGC 7023 and Orion's Veil. A final correction is needed also for the SH data arising from the difference in flux measurements with respect of the LL data. Using the flux of the 11.2 μm feature from NGC 7023 in both LL and SH modes we find this additional factor to be $\sim$3. Given that the mismatch between the resolution of our G_0 maps and the C_{60} and PAH intensity maps, we re-project and convolve the intensity maps to the PACS 160 μm resolution, which is the same as the resolution of our G_0 maps.

In order to calculate the total intensity of C_{60} and PAHs at the position of the corresponding PDRs, we measure $I_{18.9}$, I_{PAH} and I_{FIR} at the position were the combined emission from the available PAH bands peaks. We need to include the contributions to $I_{C_{60}}$ from the bands at 8.5 and 7.0 μm which are hidden under PAH emission and the 17.4 μm, which has some contribution from PAH emission. Considering a first order approximation, we use a value of 0.6 for the ratio of the 17.4 and 18.9 μm band intensities (Peeters et al. 2012), and 0.4 for the ratio of both the 7.0 and 8.5 μm with respect to 18.9 μm (Berné & Tielens 2012). The exact value of these ratios, however, is not precisely determined (Bernard-Salas et al. 2012), but even when considering other calculated values for the intrinsic rates, we find differences of at most a factor of two.

Using the carbon fractions derived in the previous section, we compare the results for our sources with other values found in the literature. In NGC 7023 the observation of growth in C_{60} ranges from 10^{-5} to 10^{-4} (Berné & Tielens 2012). A study of C-rich, H-poor PNe by García-Hernández et al. (2011) shows a range in the carbon fraction in C_{60} from 3×10^{-5} up to 3×10^{-3}, with most objects falling in the range of $\sim 10^{-4}$. All these previous estimates include the contributions to $I_{C_{60}}$ from the bands at 17.4, 8.5 and 7.0 μm. The value of f_C in all PDRs considered here fall within 3×10^{-5}–6×10^{-4}, which is in good agreement with the values found in the aforementioned studies.

The results of f_C for both PAHs and C_{60} in the different PDRs with respect to $G_0/n(\mathrm{H})$ are presented in Fig. 2.11. For PAHs, a decrease can be observed with increasing $G_0/n(\mathrm{H})$ — in regions where $G_0/n(\mathrm{H}) < 1$ — from $f_C \simeq 0.08$ until $f_C \simeq 0.01$.

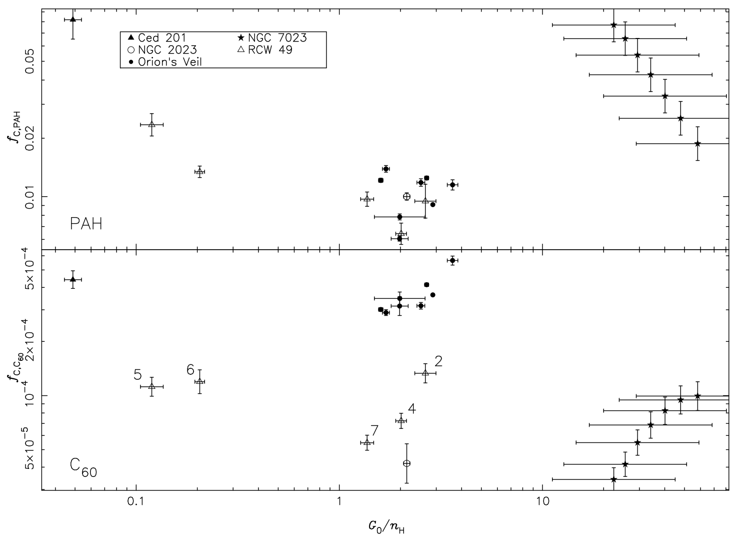

Figure 2.11.: Variations of the carbon fraction locked in PAHs (top) and C_{60} (bottom) with respect to $G_0/n(\mathrm{H})$. The different symbols indicate the different PDRs included in this work for which C_{60} is detected. For RCW 49, the numbers correspond to the individual regions considered.

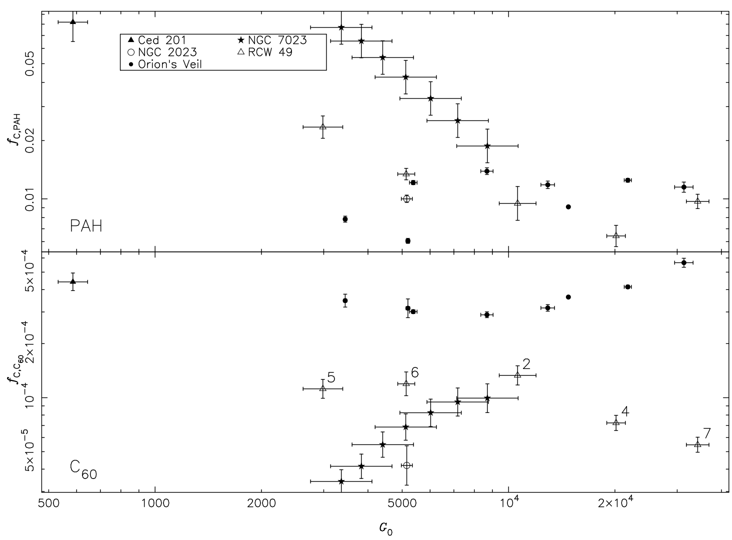

Figure 2.12.: Variations of the carbon fraction locked in PAHs (top) and C_{60} (bottom) with respect to G_0. The different symbols indicate the different PDRs included in this work for which C_{60} is detected. For RCW 49, the numbers correspond to the individual regions considered.

For $G_0/n(\mathrm{H})$ within 1–4 there is substantial scatter, even within single sources. In contrast, NGC 7023 shows a clear trend, with higher abundance than in other regions for $G_0/n(\mathrm{H})$ between 10 and 100. The behavior observed in NGC 7023 is similar that observed for the other regions in the range of $G_0/n(\mathrm{H}) < 1$.

For C_{60} no general trend that can be applied to all the regions can be observed. However, within individual objects, there is an increase in the abundance in RCW 49, NGC 7023 and Orion's Veil. In the case of RCW 49 the increase in abundance does not apply for the full range. For $G_0/n(\mathrm{H}) < 1$ the abundance of C_{60} within RCW 49 appears to remain constant. Furthermore, even for $G_0/n(\mathrm{H}) > 1$ the trend is not as clear, particularly considering that it includes regions 2 and 4, which have poorly determined hydrogen densities. In NGC 7023 and Orion's Veil the increase holds for the full probed range, although none of these regions has $G_0/n(\mathrm{H}) < 1$. We cannot conclude if this behavior applies as well for NGC 2023 or Ced 201 since we have single points for these PDRs.

Figure 2.12 shows again f_C variations of both species, in this case with respect to G_0 alone. For the PAHs fractions, a decrease in abundance is observed in NGC 7023 and, to a lesser extent, in RCW 49. The abundance in Orion's Veil is consistent with a fairly constant value. The case of C_{60} abundance again shows trends within individual regions. In NGC 7023 and Orion's Veil there is an increase in C_{60} abundance along the probed range. In Orion's Veil this increase is observed at $G_0 > 10^4$, while for NGC 7023 the increase seems to halt when G_0 approaches 10^4. On the other hand, RCW 49 shows a decrease in C_{60} abundance, which also begins at $G_0 \sim 10^4$.

2.5. Discussion

By examining Figs. 2.11 and 2.12, we conclude that within NGC 7023, there is a clear trend for a decrease in PAH abundance and an increase in C_{60} abundance with increasing $G_0/n(\mathrm{H})$ (or with increasing G_0 as the density is constant). The other regions show a more mixed behavior. In RCW 49, for example, the PAH abundance decreases with increasing $G_0/n(\mathrm{H})$ or G_0, but the trend in the C_{60} abundance is less clear. In contrast, for Orion's Veil, there is no clear trend in the PAH abundance but a hint of an increase in the C_{60} abundance with $G_0/n(\mathrm{H})$, while the trend with G_0 is unclear for both species. We attribute the distinctiveness of the trend in NGC 7023 to the fact that the PDR is seen edge-on, while for other regions the morphological and geometrical characteristics are more uncertain and might play a role in the observed trends or lack thereof. Combining all sources together there is no obvious trend for either species with respect to $G_0/n(\mathrm{H})$ or G_0. From this, we conclude that besides the physical conditions — G_0 and $n(\mathrm{H})$ — there must be other parameter(s) influencing the evolution of PAHs and fullerenes.

The clear trends in the PAH and fullerene abundances with G_0 in NGC 7023 have been interpreted in a simple model, describing the chemical evolution of PAHs under the influence of the stellar UV photons through H-loss to graphene sheets resulting ultimately, on the one hand, into small hydrocarbons due to C_2 fragmentation and, on the other hand, to fullerenes through isomerization (Berné & Tielens 2012). We note that time is an additional factor entering such chemical models. Specifically, H-loss is expected to be described by a balance between collisional hydrogenation and UV-driven dehydrogenation and thus regulated by G_0 and n(H). However, C_2-loss is likely to be a time-dependent process controlled by G_0. Hence the absence of a general trend in the PAH and fullerene abundances across many sources is not to be expected. Moreover, it should be realized that PAH fragmentation and fullerene formation are only connected for PAHs in excess of at least 60 C-atoms.

PAH abundance appears to be related to the age of the PDRs. We observe the highest PAH abundance in Ced 201 and NGC 7023, the youngest sources in our sample, with their ages estimated to be 1500 and 10^5 yr, respectively (Alecian et al. 2008). For the remaining PDRs we find similar, overlapping age estimates: 1–7 Myr for NGC 2023 (López-García et al. 2013), 2–3 Myr for RCW 49 (Piatti et al. 1998) and 1–3 Myr for Orion's Veil (Flaccomio et al. 2003). For these PDRs we find a lower abundance of PAHs than in Ced 201 or NGC 7023, which is consistent with a time-dependent destruction of PAHs.

Recently, the first step in the processing from PAHs to fullerenes has been modeled in detail by Montillaud et al. (2013). The results of this model are shown in Fig. 2.13. To the left of this figure, PAHs are fully hydrogenated while to the right they are expected to fully dehydrogenated — i.e. graphene flakes. More specifically, the lines in this figure represent the loci at which the hydrogenation balance leads to a constant H-fraction on a PAH of a given size. So, the further to the right, the more of the initial PAH size distribution will be destroyed but as long as the PAH size distribution extends to $\sim$100 C-atoms, some fraction of the PAHs will remain hydrogenated. The different sources in our sample are indicated by symbols in this figure. We note that the sources without detectable C_{60} are to the left of the "stability-line" for PAHs in excess of 60 C-atoms, leading some credence to a photochemical transformation model of PAHs into fullerene in the ISM. However, the C_{60}/PAH abundance ratio does not correlate well with the "depth" into the fully dehydrogenated zone. This may merely indicate that time is of the essence or that there are fluctuations in the size distribution of the PAH family from region to region. Ced 201 forms an interesting exception to this as it has C_{60} despite being in the "stable-zone" for PAHs with more than 60 C-atoms. This is a very peculiar source as it is a chance encounter of the illuminating star with a cloud. This star-cloud interaction seems to have lead to a shock wave (Cesarsky et al. 2000) located in the position where the C_{60} abundance is particularly high. Hence, it is tempting to speculate that in this particular source C_{60} is formed by shock processing of PAHs and/or dust grains. The inferred shock velocity is quite low ($\sim$10 km s^{-1} Witt et al. 1987) and such low velocity shocks are not expected to lead to much PAH destruction (Micelotta et al. 2010). However, observed C_{60}/PAH abundance is only 0.005 and thus little processing is required.

Finally, small HAC grains have also been considered as photochemical starting points for C_{60} formation in the ISM. The general process involved is the same: the first step requires dehydrogenation of the HAC particles followed by a shrinking of the resulting cage (Micelotta et al. 2012). As for PAHs, the hydrogenation of HAC is set by a balance between reactions with H and photochemical H-loss (Mennella et al. 2001, 2002; Mennella 2006) and therefore controlled by G_0/n(H) (Chiar et al. 2013). The

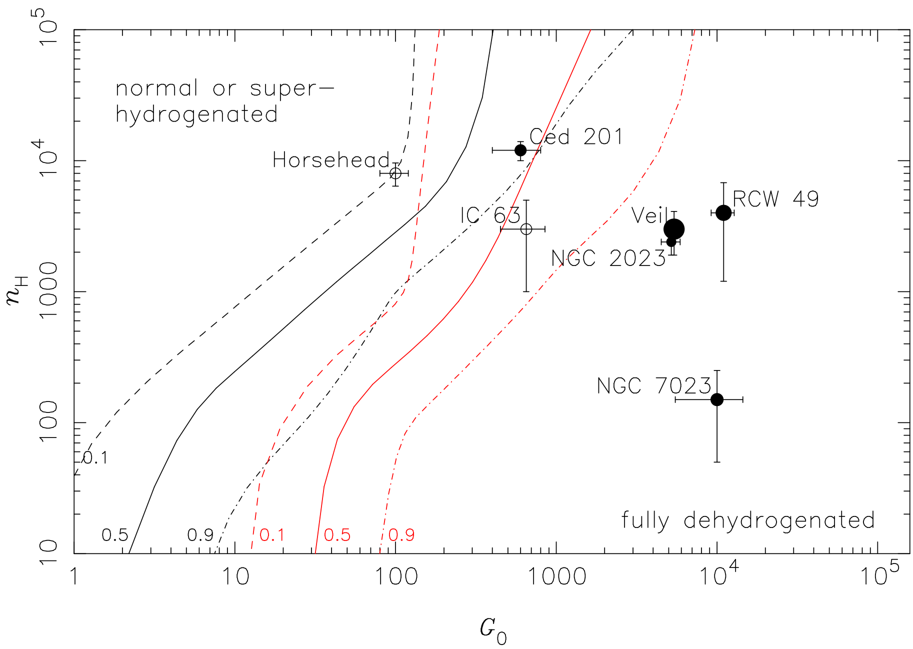

Figure 2.13.: Hydrogenation state of circumcoronene ($C_{54}H_{18}$; black) and circumovalene ($C_{66}H_{20}$; red) as function of G_0 and the atomic hydrogen density. The labels of the lines indicate the fraction of the respective molecules that is fully dehydrogenated. The full circles correspond to the PDRs where we detect C_{60}, the symbol size is proportional to the C_{60}-to-PAH ratio. The sources for which we can only derive upper limits are marked by open circles. The error bars mark the ranges for the physical conditions. The data on hydrogenation states of $C_{54}H_{18}$ and $C_{66}H_{20}$ were taken from Montillaud et al. (2013).

main difference with the PAH model resides in the timescale for C-loss. Based upon molecular dynamics calculations (Zheng et al. 2007), this C-loss timescale is calculated to equal the IR-cooling timescale at 100–200 K for HACs and such a low temperature is readily attained by HAC grains containing ~500 C-atoms (or less). However, the adopted C-binding energies are only 0.36 eV (Micelotta et al. 2012), which is much less than expected for carbon cages. As emphasized in the original molecular dynamics study, these results may not be statistically significant (Irle, S., private communication, Zheng et al. 2007). Further laboratory studies will have to settle this issue.

2.6. Conclusions

We present a survey of C_{60} in PDRs. While in NGC 2023 the presence of fullerenes had already been established (Sellgren et al. 2010; Peeters et al. 2012), the detection on RCW 49 and Ced 201 represent new sources where C_{60} is confirmed to be present. We also quantified its abundance as a fraction of elemental carbon and found values consistent with other studies of C_{60} in PDRs, with values ranging from $\sim 3 \times 10^{-5}$ to $\sim 6 \times 10^{-4}$. Furthermore, the values we derive for T_d from FIR observations indicate that these regions have temperatures ranging from 20 to 40 K, which is too low for C_{60} to be emitting in grains, and supports the idea of a gas phase species or small sized clusters undergoing stochastic heating (Sellgren et al. 2010). The well-known strong IR bands at 6.2, 7.7, 8.6, 11.2, 12.7 and 16.4 μm, show a very similar spatial behavior, with only minor variations in all sources. In contrast, the spatial distribution of the 18.9 μm band is very different and we conclude that this band has a different carrier (i.e., C_{60} Cami et al. 2010; Sellgren et al. 2010) than the other bands (i.e.. PAHs).

While some of the sources appear to show trends in C_{60} and PAH abundance, we find universal dependence with either $G_0/n(\mathrm{H})$ or G_0 when considering all PDRs together. We consider age as a factor explaining the lack of a general trend. Comparing our observational results to the model predictions of Montillaud et al. (2013) for PAH dehydrogenation, we find that regions where C_{60} is detected have physical conditions consistent with full dehydrogenation of PAHs of at least 60 C-atoms, with the exception of Ced 201. The conditions of regions where only upper limits for C_{60} abundance could be derived, are consistent with only partial dehydrogenation of PAHs with relevant sizes. These results support models where the dehydrogenation of carbonaceous species is the first step towards C_{60} formation (Berné & Tielens 2012; Micelotta et al. 2012).

More observations aimed at measuring variations of C_{60} abundance with respect to both PAHs and HAC, as well as better determinations of $n(\mathrm{H})$ are needed to confirm the reality of these trends and the more likely parent species. Better constraints on the age estimates and the study of additional PDRs with significant age differences are needed to test our hypothesis about the effect of age in generating the seemingly independent trends for each PDR.

Acknowledgments

Studies of interstellar chemistry at Leiden Observatory are supported through the advanced-ERC grant 246976 from the European Research Council, through a grant by the Dutch Science Agency, NWO, as part of the Dutch Astrochemistry Network, and through the Spinoza premie from the Dutch Science Agency, NWO. PC acknowledges support from a Huygens fellowship at Leiden University. We would like to thank B. Ochsendorf and H. Andrews for facilitating us their reduced spectra of B 33 and IC 63 respectively. We would also like to thank J. Montillaud for the data on dehydrogenation state of PAHs. We also acknowledge the anonymous referee, whose comments helped us in improving this paper.

This work is based in part on observations made with the *Spitzer Space Telescope*, which is operated by the Jet Propulsion Laboratory, California Institute of Technology under a contract with NASA.

The *Herschel* spacecraft was designed, built, tested, and launched under a contract to ESA managed by the Herschel/Planck Project team by an industrial consortium under the overall responsibility of the prime contractor Thales Alenia Space (Cannes), and including Astrium (Friedrichshafen) responsible for the payload module and for system testing at spacecraft level, Thales Alenia Space (Turin) responsible for the service module, and Astrium (Toulouse) responsible for the telescope, with in excess of a hundred subcontractors.

PACS has been developed by a consortium of institutes led by MPE (Germany) and including UVIE (Austria); KU Leuven, CSL, IMEC (Belgium); CEA, LAM (France); MPIA (Germany); INAF-IFSI/OAA/OAP/OAT, LENS, SISSA (Italy); IAC (Spain). This development has been supported by the funding agencies BMVIT (Austria), ESA-PRODEX (Belgium), CEA/CNES (France), DLR (Germany), ASI/INAF (Italy), and CICYT/MCYT (Spain).